Imperial College London

Literature Review: Characterisation of proton Bragg peak using novel scintillating fibre design for use in proton beam therapy facility (LhARA)

Anthea E. MacIntosh-LaRocque

Student's CID: 01507986
Project code: HEPH-Long-1
Supervisor: Prof. Kenneth Long
Assessor: Dr. Jaroslaw Pasternak
Word count: 2492

Submitted for the FHEQ Level 7 module PHYS70002 - Physics MSci Project 2022-2023 in the Department of Physics at Imperial College London. October 2022

Abstract

LhARA is a proposed proton beam therapy research facility. This project aims to develop the SmartPhantom, a piece of instrumentation which will provide online dose mapping for proton beams at LhARA, integrating ionacoustic and scintillating fibre technology to achieve this. This review presents the physics of ionacoustic and scintillating fibre detectors alongside state-of-the-art research into these technologies. Alternative dose mapping techniques are also reviewed.

1 Introduction

Cancer directly affects one in five individuals in their lifetime, with one in ten dying from the disease [1]. Radiotherapy is widely prescribed to treat cancer [2]. Proton beam therapy (PBT) is a form of radiotherapy with advantages such as maximising tumour damage while sparing healthy tissue [3][4]. More research is required to understand the biological processes underpinning PBT. The Laser-hybrid Accelerator for Radiobiological Applications (LhARA) [5] is a proposed PBT research facility. Fig. 1 shows a render of the facility. It is imperative that online dose mapping of the beam used at LhARA can be realised for beam quality assurance and to relate dose deposition to the observed biological effects. SmartPhantom [6] is an online dose mapping technology being developed for LhARA which combines two emerging dosimetry techniques: ionacoustics and scintillating fibres.

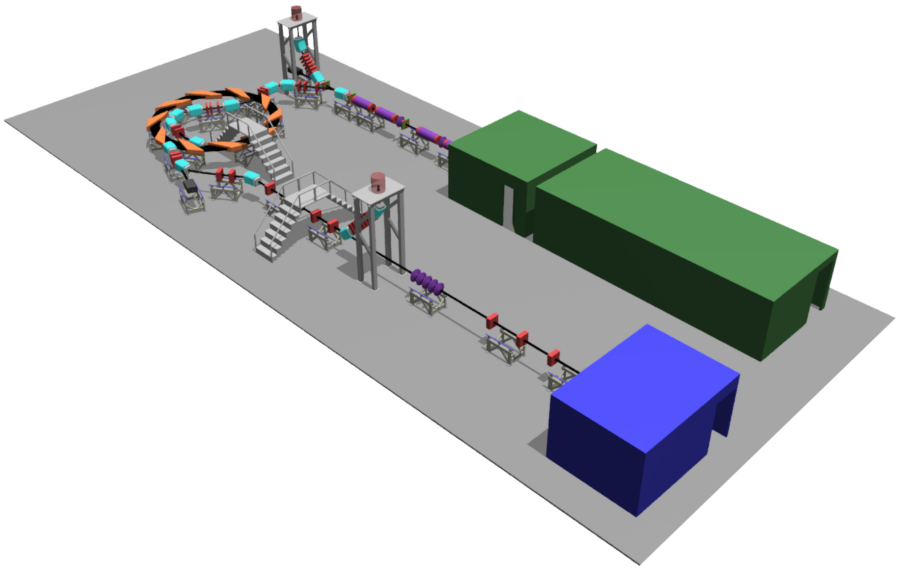

Figure 1: A render of the proposed LhARA facility. Image from [5].

This project continues SmartPhantom's development, with a focus on scintillating fibre technology. This review presents the foundational physical understanding and wider context required for this project, including proton-matter interactions, PBT, ionacoustic and scintillating fibre technologies. The current state-of-the-art in ionacoustic and scintillating fibre technologies is presented. Other techniques used for PBT dosimetry are surveyed, drawing comparisons to ionacoustic and scintillating fibre detectors.

2 Background

2.1 Interactions between protons and matter

When protons have enough kinetic energy to induce ionisation within matter, they are considered *directly ionising radiation*. Direct ionisation occurs because the particle incrementally loses energy while travelling through matter, emitting *bremsstrahlung radiation*. If the electron ejected by ionisation has sufficient energy, a secondary electron track may be created. If there is insufficient energy to induce complete ionisation, an electron may be excited to a higher atomic energy level [7].

The three primary proton-matter interactions are *stopping*, *multiple Coulomb scattering* (MCS) and *hard scattering* [8]. Stopping denotes protons losing energy and coming to rest due to multiple electromagnetic (EM) interactions with atomic electrons and, to a lesser extent, nuclei. The *continuous slowing down approximation* is a theoretical model which calculates the rate of energy loss and range of fast charged particles in matter. MCS describes the random deflection of protons by EM interactions with atomic nuclei and electrons [8]. Hard scattering refers to a single hard scatter of a proton by EM or nuclear forces, distributing dose at large distances from the target atom. The rate of energy loss per unit path length is known as *stopping power*. For charged particles, stopping power is proportional to the square of the particle's charge and inversely proportional to its velocity squared. As the particle comes to rest, it deposits more energy per unit length in matter, causing more ionisation and dose. The stopping of protons results in a reduced flux of protons upstream. Fewer protons results in fewer statistical variations in proton range, and thus a sharper peak in deposited energy or *Bragg peak*, as shown in Fig. 2 [7][9].

The range-energy relation between charged particles and matter can be described by

$$\left\langle -\frac{dE}{dx} \right\rangle = K z^2 \frac{Z}{A} \frac{1}{\beta^2} \left[\frac{1}{2} \ln \frac{2 m_e c^2 (\beta\gamma)^2 W_{\max}}{I^2} - \beta^2 - \frac{\delta(\beta\gamma)}{2} \right], \tag{1}$$

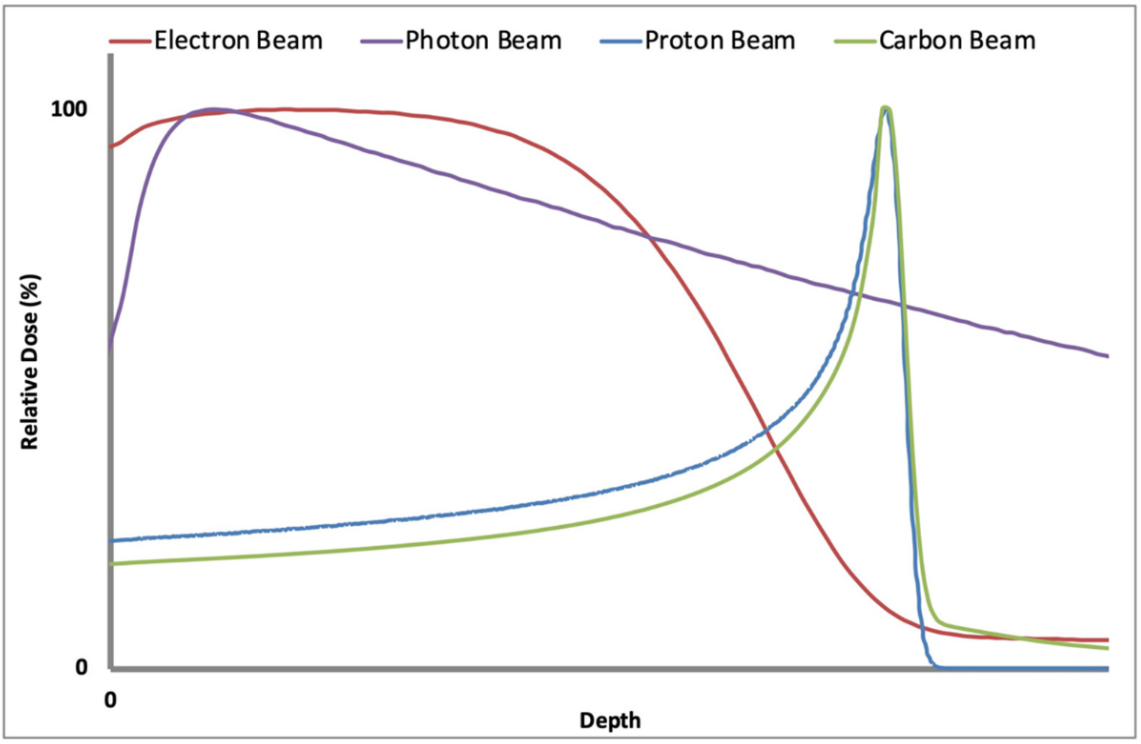

Figure 2: The relative dose-depth profiles of electrons (red curve), photons (purple curve), protons (blue curve), and carbon ions (green curve). From [9].

known as the the Bethe-Bloch Equation, with symbols defined in Table 1 [10]. This equation is not valid at very high energies, where spin becomes important [11].

An analytical approximation to the Bragg curve for protons and heavy ions, valid for energies between 10 and 200 MeV, is provided in Bortfeld, 1997 [12],

$$D(z) = \Phi_0 \frac{e^{-\xi^2/4}\sigma^{1/p}\,\Gamma(1/p)}{\sqrt{2\pi}\rho p \alpha^{1/p}(1+\beta R_0)} \left[\frac{1}{\sigma}\mathscr{D}_{-1/p}(-\xi) + \left(\frac{\beta}{p} + \gamma\beta + \frac{\epsilon}{R_0}\right)\mathscr{D}_{-1/p-1}(-\xi)\right], \qquad (2)$$

with parameters and constants defined in Table 2.

2.2 Proton beam therapy

Radiotherapy is a common cancer treatment [2]. *Conventional radiotherapy* irradiates tumour cells with photon or electron beams to elicit strand breaks in the tumour cells' DNA. The primary challenge in radiotherapy is minimising healthy tissue damage [15]. As shown in Fig. 2, photon and electron beams deliver the most dose close to the tissue surface which is undesirable

Table 1: Summary of parameters and constants in Equation 1 [10]

Symbol	Definition	Value/Unit
K	$4\pi N_A r_e^2 m_e c^2$	
N_A	Avogadro's number	$6.022 \times 10^{23}\,\mathrm{mol}^{-1}$
r_e	classical electron radius	2.82 fm
z	charge number of incident particle	
Z	atomic number of absorber	
A	atomic mass of absorber	$\mathrm{g\,mol}^{-1}$
$m_e c^2$	electron mass $\times c^2$	0.511 MeV
β	v/c	
v	speed of incident particle	$\mathrm{m\,s}^{-1}$
γ	Lorentz factor, $1/\sqrt{1-v^2/c^2}$	
$W_{\max}$	maximum possible energy transfer to an electron in a single collision	MeV
I	mean excitation energy	eV

Table 2: Summary of parameters and constants required for the analytic approximation of the Bragg curve [12]

Symbol	Description	Value	Unit
Φ_0	Primary fluence		cm^{-2}
ξ	Substitution to simplify expression	$(R_0 - z)/\sigma$	1
z	Depth		cm
R_0	Range	αE_0^p	cm
σ	Width of Gaussian peak	$\sqrt{\left(\sigma_{\mathrm{mono}}^2 + \sigma_{E,0}^2 \alpha^2 p^2 E_0^{2(p-1)}\right)}$	cm
σ_{mono}	Width of Gaussian range straggling	$0.012 R_0^{0.935}$	cm
$\sigma_{E,0}$	Width of Gaussian energy spectrum	$\approx 0.01 E_0$	MeV
p	Exponent of energy range relation	1.77	1
α	Proportionality factor	0.0022	$\mathrm{cm\,MeV}^{-p}$
E_0	Initial beam energy		MeV
ρ	Mass density of medium		$\mathrm{kg\,cm}^{-3}$
$\Gamma(x)$	Gamma function	$\int_0^\infty x^{z-1} e^{-x} dx$ [13]	1
$\mathscr{D}(x)$	Parabolic cylinder function	See [14]	1
β	Slope parameter of fluence reduction relation	0.012	1
γ	Fraction of locally absorbed energy released in nonelastic nuclear interactions	0.6	1
ϵ	Fraction of primary fluence contributing to the tail of the energy spectrum	$\approx$ 0.0 - 0.2	1

for tumours located deeper within the tissue. PBT and heavy ion radiotherapy (HIRT) provide promising alternatives to conventional radiotherapy due to their spatially localised energy deposition, although the biology underlying PBT is not well understood [16] [17] [3] [4].

2.3 Ionacoustics

When ionising radiation deposits energy in matter, the energy deposition elicits a local temperature increase and thermal expansion of matter, causing a detectable pressure pulse from the interaction site [18]. The pressure $p(\mathbf{r},t)$ induced in water by temperature increase $T(\mathbf{r},t)$ propagates as

$$\left(\nabla^2 - \frac{1}{v_s^2}\frac{\partial^2}{\partial t^2}\right) p\left(\mathbf{r},t\right) = -\frac{\beta}{\kappa v_s^2}\frac{\partial^2 T\left(\mathbf{r},t\right)}{\partial t^2}, \tag{3}$$

where v_s is the acoustic speed of sound in water, β is the coefficient of volumetric expansion and κ is the isothermal compressibility [18]. Thermal and stress confinement conditions allow for the heat equation to be written as

$$\rho c_V \frac{\partial T(\mathbf{r},t)}{\partial t} = H(\mathbf{r},t), \tag{4}$$

where ρ is the mass density, c_V is the specific heat capacity at constant volume, and $H(\mathbf{r},t) = Q(\mathbf{r})H'(t)$ is the spatially and temporally separable heating function. Thermal confinement implies that the duration of heat diffusion is much greater than the proton stopping time. Stress confinement implies that the proton pulse takes less time than the pressure-induced volume expansion. Using Equation 4, Equation 3 can be solved for $p(\mathbf{r},t)$:

$$p(\mathbf{r},t) = \frac{\beta}{4\pi v_s \kappa \rho c_V}\frac{\partial}{\partial t}\int_{A(t)}\frac{Q(\mathbf{r}')}{R}dA', \tag{5}$$

where $Q(\mathbf{r}')$ is the deposited energy density, $R = |\mathbf{r} - \mathbf{r}'|$, and $A(t)$ is the surface over which $R = v_s t$ [18]. This acoustic signal can be converted to an electrical one by a transducer. When displayed as a function of time, this signal is denoted a time-series. Algorithms can reconstruct the initial pressure distribution from the time-series, recovering the initial dose distribution. Such algorithms include universal back-projection, Fourier transform, (iterative) time reversal and inversion of the linear Radon transform [19][20][21][22][23]. A typical ionacoustic set-up is shown in Fig 3.

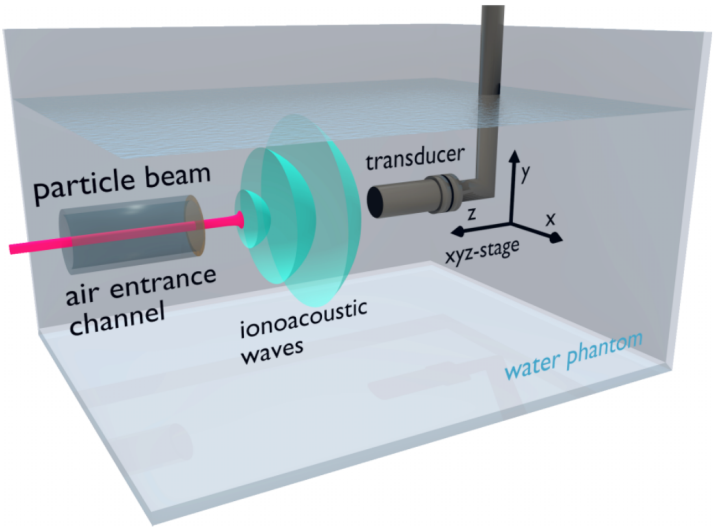

Figure 3: Typical ionacoustic set-up. From [24].

2.3.1 Ionacoustic research at Ludwig Maximilian University of Munich

Lascaud, Dash et al., 2021 [25] presents a linear sensor array for dose mapping of 20 MeV and 22 MeV proton beams in a water phantom. The sensor comprises between 5 and 200 elements, with a maximum length of 4 cm. While the Bragg peak range could be determined accurately, the lateral resolution of the dose map is poor (>10% relative error) due to a limited field-of-view (FOV). For homogeneous phantoms, range verification accuracy is primarily limited by the detector's sampling frequency. This research also found that the Bragg peak of a long-duration proton pulse can be artificially spread out during reconstruction because the duration of the pulse influences the frequency content of the resultant signal. In pre-clinical studies, this can be mitigated by a simple alignment procedure. The authors suggest using two imaging devices with different FOV simultaneously to solve the issue of requiring a small FOV to obtain good lateral resolution, whilst also needing a large FOV to detect signals at <50 kHz.

Lascaud et al., 2019 [26] presents the novel use of a Capacitive Micromachined Ultrasonic Transducer (CMUT) for ionacoustic detection. The CMUT was able to detect ionacoustic signals at far lower frequencies (hundreds of kHz) than conventional PZT transducers can achieve. Lascaud et al., 2021 [27] evaluates the impact of the backing material and detector geometry on detector sensitivity and accurate dose mapping. Findings suggest that a tungsten

backing is advantageous over an epoxy backing.

2.4 Scintillating fibres

2.4.1 Fundamentals

Scintillating fibres are commonly used to detect charged particle radiation. There are three main processes which contribute to the emission of detectable radiation in a scintillator: fluorescence, phosphorescence and delayed fluorescence [28]. Fluorescence is the excitation of molecules within the scintillating material followed by the prompt emission of visible radiation. Delayed fluorescence has a longer emission time following excitation. In contrast, phosphorescence results in the emission of light with a longer wavelength and slower characteristic emission time than fluorescence.

There are two broad classes of scintillating material: organic and inorganic [28]. This review focuses on organic scintillators. Organic scintillation materials typically have the π-electron structure shown in Fig. 4 [28]. At room temperature, molecules typically sit in the lowest vibrational state of the ground electronic singlet state, level S_{00}. If the molecule is excited to any higher singlet state, it will be de-excited to S_1 by non-radiating internal conversion. Radiation denoted "prompt fluorescence" comes from the relaxation of the molecule from the S_{10} state to any S_0 state [28]. The prompt fluorescent intensity due to this decay can be described as a function of time as

$$I = I_0 e^{-t/\tau}, \tag{6}$$

where I_0 is the maximum intensity and τ is the prompt fluorescent decay time ($\tau \sim 1\,\text{ns}$) [28].

2.4.2 Scintillation efficiency and quenching

Scintillation efficiency is defined as the fraction of energy from the incident particle which is converted to detectable light.

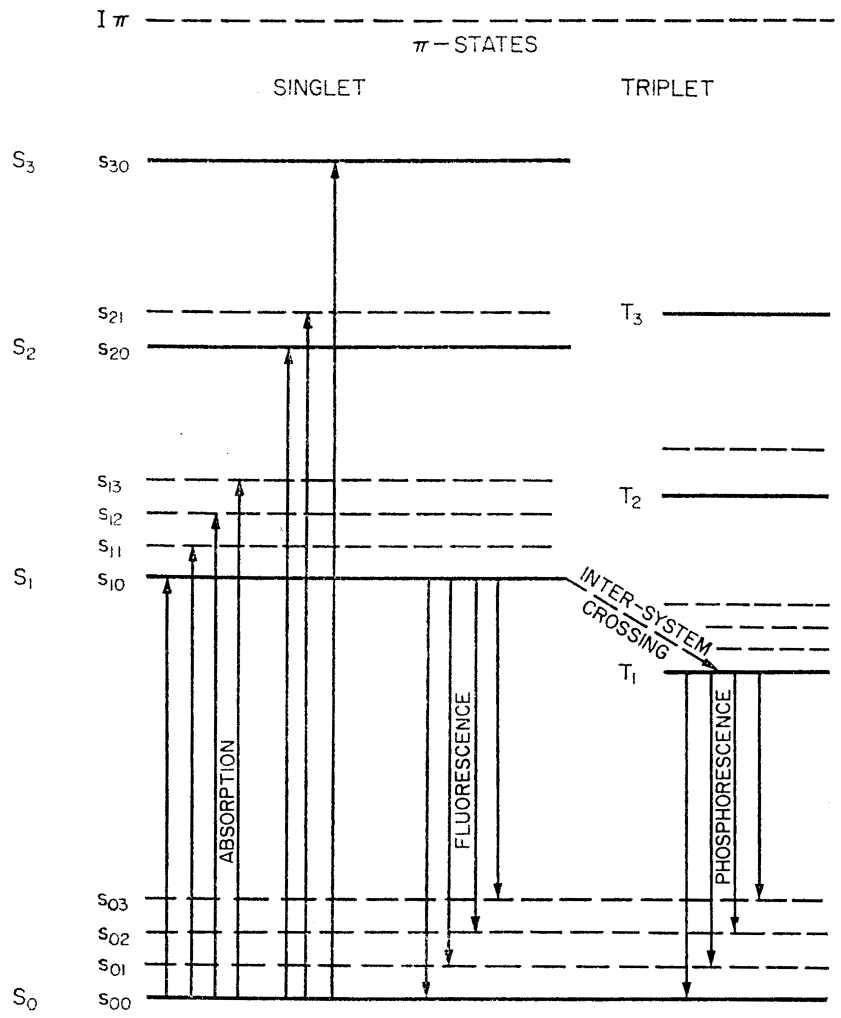

Figure 4: π-electronic energy levels. From [29]

Self-absorption is the process by which light emitted by a scintillator is reabsorbed by the scintillating material [28]. This occurs when the energy released as fluorescence is greater than or equal to the energy required for the absorption pathways of the electronic structure. The only decay mode of the π-electron structure satisfying this condition is the $S_{10} \rightarrow S_{00}$ mode which overlaps with the $S_{00} \rightarrow S_{10}$ mode. Therefore organic scintillators exhibit limited self-absorption.

Scintillation efficiency can also be degraded by de-excitation modes called "quenching effects" which do not result in the emission of light [28].

A scintillator's response is described by relating the fluorescent energy emitted per unit path length dL/dx to the energy loss per unit path length dE/dx. Assuming there is no quenching,

the assumption that that light yield is proportional to energy loss can be made, hence

$$\frac{dL}{dx} = S\frac{dE}{dx}, \tag{7}$$

where S is the scintillation efficiency [28]. To account for quenching effects in this relation, the following procedure was suggested by Birks [29]. It is assumed that scintillation efficiency is lowered by quenching from damaged molecules and that the density of damaged molecules is proportional to the ionisation density dE/dx. Hence the density of damaged molecules is $B(dE/dx)$, with proportionality constant B. Only a fraction, k, of the damaged molecules cause quenching. Thus Equation 7 is amended to give Birks' law [29],

$$\frac{dL}{dx} = \frac{S\frac{dE}{dx}}{1 + kB\frac{dE}{dx}}. \tag{8}$$

For small dE/dx, this reduces to Equation 7. Unlike electrons, protons do not exhibit a linear response due to their higher LET. For protons, alternative equations have been proposed to fit empirical findings. Craun & Smith [30] propose the relation,

$$\frac{dL}{dx} = \frac{S\frac{dE}{dx}}{1 + kB\frac{dE}{dx} + C\left(\frac{dE}{dx}\right)^2}, \tag{9}$$

where C is an empirically determined parameter. For small dE/dx, this reduces to Equation 8. Kelleter & Jolly, 2020 [31] introduces a model which describes the depth-light curve in a quenching scintillator by combining Birks' law [29] and Bortfeld's equation [12].

2.4.3 Light collection

Following scintillation, light generated in the material must be transported through the scintillator to a photomultiplier tube (PMT) or other sensor. Here, we will focus on using scintillating fibres (thin tubes of scintillating material, often enclosed in cladding to enhance total internal reflection (TIR)) for light collection. In scintillating fibres, light is transported down the fibre by reflections on the surface of the fibre. A diagram of a scintillating fibre is shown in Fig. 5 [28].

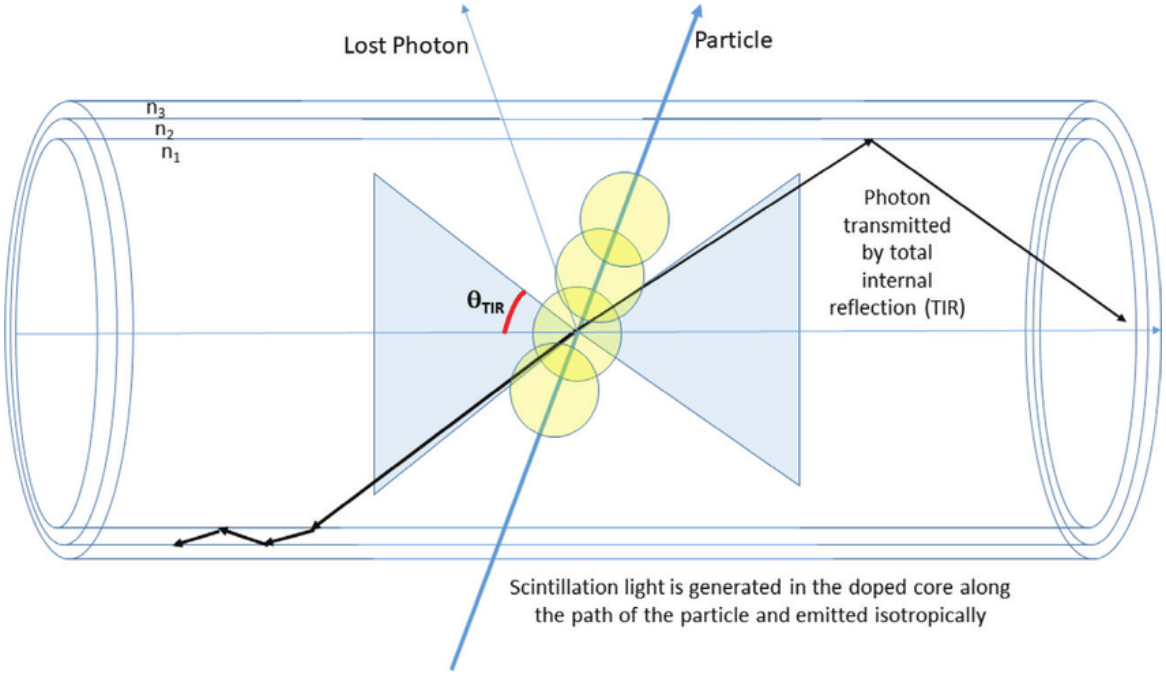

Figure 5: Diagram of a scintillating fibre. n_i are the refractive indices of the core and cladding layers. θ_{TIR} is the maximum angle for TIR. From [32].

Energy resolution is maximised by maximising the number of scintillation photons collected by the PMT or sensor [28]. Therefore light attenuation during collection must be minimised. Light attenuation results from imperfections at the core-cladding interface, self-absorption and Rayleigh scattering in the core [28].

In a typical scintillation pulse fewer than 10 photons are collected by the PMT or sensor because the fibres themselves are thin, so little ionisation occurs, and even fewer photons are able to reach the PMT due to attenuation [28]. Thus minimising the sensor's noise level is essential to distinguishing signal from noise.

TIR must be minimised at the fibre-PMT junction. The PMT is often coupled with something close to the refractive index of glass. Thin scintillators should not be mounted directly onto the PMT; this causes drastic pulse height variations due to PMT non-uniformities [28]. A light pipe can spread out the light from each scintillation over the PMT end window to average out any non-uniformities. If the detector is likely to experience large temperature changes or vibrations, an epoxy cement can be used to couple the fibres to the PMT [28].

2.5 SmartPhantom

The LhARA facility is a forthcoming centre which will be used to study PBT [5]. SmartPhantom [6] is a piece of instrumentation in development for use at LhARA to provide reproducible and accurate online measurement of the energy deposited by proton beams in water and cell samples. The online measurement will include Bragg curve fitting, LET and dose calculations. This will be achieved using both ionacoustic and scintillating fibre detectors. A render of SmartPhantom is shown in Fig. 6. The initial design for the scintillating fibre detectors in SmartPhantom is based on the PTW-T41023 water phantom [33].

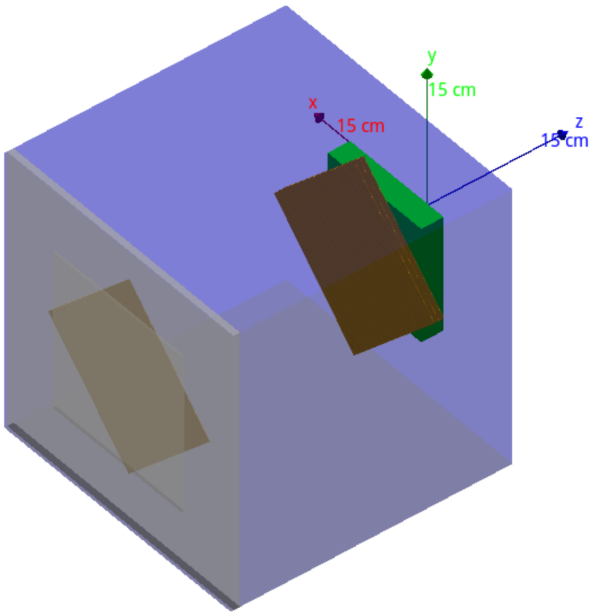

Figure 6: Render of the SmartPhantom. The brown planes represent the scintillating fibres. The blue colour shows the volume of water. The grey plane represents the plexiglass window. The green plane represents the position of the ionacoustic transducer. Image from [6].

The proton beam enters the water phantom via a plexiglass window. Inside the water phantom are multiple stations consisting of two planes of scintillating fibres suspended in the plane perpendicular to the beam's path. Clear fibres connect the scintillating fibres to a camera. Data from the camera will undergo image processing to determine the intensity and position of the beam energy deposition in the plane of the scintillating fibre planes. A transducer will sit within the phantom to detect ionacoustic signals.

Thus far, Geant4 [34] simulations have been created to model the SmartPhantom's scintillating fibre technology [6]. The Bragg curves from these simulations are shown in Fig. 7. k-Wave is software designed for time domain acoustic simulations [22]. k-Wave simulations have been created to simulate the response of ionacoustic detectors to the dose deposited by a proton beam. The Geant4 and k-Wave simulations work as a pipeline, so the results of the Geant4 simulation can be used as the input data for k-Wave.

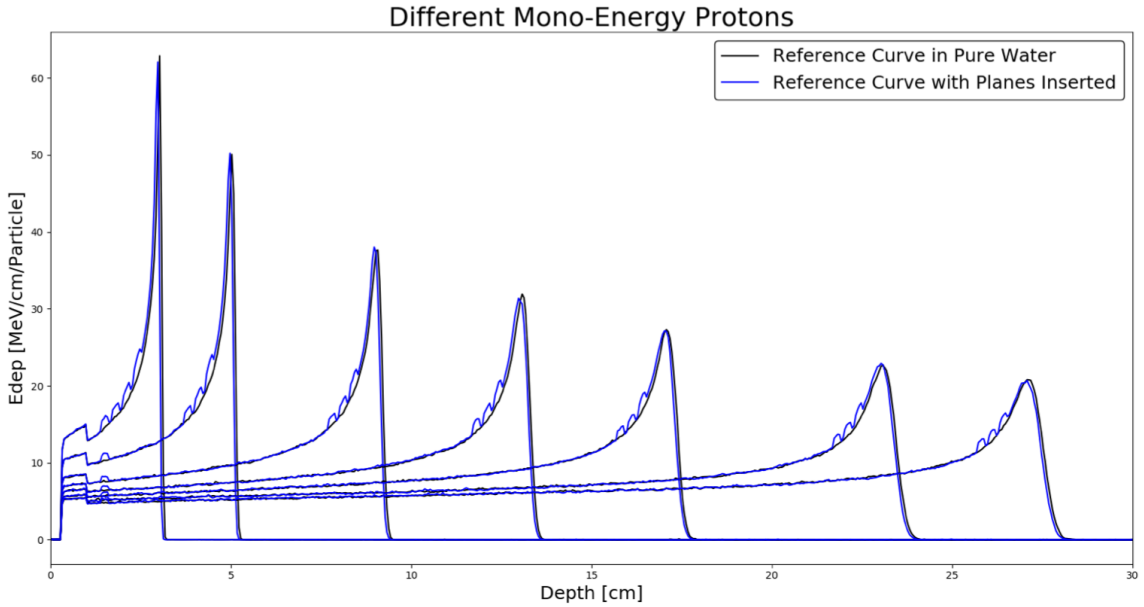

Figure 7: 60 MeV to 200 MeV proton beam depth-energy curves with and without four scintillating fibre planes. The first bump is caused by the entry window while the bumps downstream are caused by the planes. Image from [6].

2.6 Other techniques used for proton beam dosimetry

2.6.1 PET

Proton emission tomography (PET) is an emerging approach to PBT dosimetry in clinical settings. When protons interact with tissue by inelastic collisions, nuclear reactions occur, creating short-lived positron emitting isotopes [35]. A PET scan taken immediately after or during irradiation reveals the location of these positron emitters, establishing the proton beam's path [35].

Unlike in ionacoustic technology, the Bragg peak is not explicitly imaged with PET scans. The inelastic scattering which produces positron emitters occurs for proton energies higher than those resulting in the Bragg peak [35]. Hence the activity upstream of the Bragg peak is mapped before falling off rapidly at the Bragg peak allowing for the Bragg peak to be implicitly localised [35].

PET scanning can be used for either online or offline monitoring. Online monitoring suffers from reduced detector sensitivity and a reduced FOV [35]. Moreover, there can be geometrical problems from the beam and detector orientation which interferes with the 3D image acquisition [35]. During offline monitoring, the patient is moved to a PET scanner following treatment. The delay in obtaining the scan can result in positron emitters decaying or being transported away from their initial location [35].

2.6.2 Film dosimetry

Film dosimetry begins by coating a transparent polymer base with a colourless polymer sensor film (∼100 µm thick) which acts as a tissue-equivalent detector [36]. The film turns deep blue upon irradation. The optical density of the blue tint corresponds to the radiation dose the film has received [36]. Evidence is emerging that this can be used for heavy ion dosimetry [37].

2.6.3 Ionisation chambers

Ionisation chambers are the industry standard for dosimetric measurements [38]. This is done by measuring the charge created as a result of the interaction between ionising radiation and matter. Calibration is used to determine the deposited dose, which induces uncertainty into measurements [39]. Ionisation chambers can be made with tissue-equivalent materials which is advantageous [39].

3 Conclusions

This review summarised how proton-matter interactions are harnessed to provide clinical proton beam mapping with ionacoustic and scintillating fibre detectors. SmartPhantom will combine these techniques to provide online dosimetry. Existing simulations, alongside experiments at Ludwig Maximilian University of Munich, will provide the foundations for the continued development of the SmartPhantom. Other techniques used for proton beam dosimetry possess advantages such as tissue-equivalent absorption and online operation. Disadvantages of some of the techniques include uncertainty induced by calibration and delayed mapping.

References

[1] J. Ferlay, M. Colombet, I. Soerjomataram, D. M. Parkin, M. Piñeros, A. Znaor, and F. Bray, "Cancer statistics for the year 2020: An overview," *International Journal of Cancer*, vol. 149, no. 4, p. 778–789, 2021.

[2] M. Arruebo, N. Vilaboa, B. Sáez-Gutierrez, J. Lambea, A. Tres, M. Valladares, and A. González-Fernández, "Assessment of the Evolution of Cancer Treatment Therapies," *Cancers*, vol. 3, no. 3, p. 3279–3330, 2011. [Online]. Available: https://dx.doi.org/10.3390/cancers3033279

[3] Y. Prezado and G. R. Fois, "Proton-minibeam radiation therapy: A proof of concept: Proton-minibeam radiation therapy: A proof of concept," *Medical Physics*, vol. 40, no. 3, p. 031712, Feb 2013.

[4] Y. Prezado, G. Jouvion, A. Patriarca, C. Nauraye, C. Guardiola, M. Juchaux, C. Lamirault, D. Labiod, L. Jourdain, C. Sebrie, R. Dendale, W. Gonzalez, and F. Pouzoulet, "Proton minibeam radiation therapy widens the therapeutic index for high-grade gliomas," *Scientific Reports*, vol. 8, no. 1, p. 16479, Dec 2018.

[5] G. Aymar, T. Becker, S. Boogert, M. Borghesi, R. Bingham, C. Brenner, P. N. Burrows, O. C. Ettlinger, T. Dascalu, S. Gibson, and et al., "Lhara: The laser-hybrid accelerator for radiobiological applications," *Frontiers in Physics*, vol. 8, 2020.

[6] H. T. Lau, "Medical applications for particle physics," Ph.D. dissertation, Imperial College London, Feb 2022.

[7] F. M. Khan and J. P. Gibbons, *Khan's the physics of radiation therapy*, 6th ed. Philadelphia, PA [u.a.] Wolters Kluwer: J Med Phys., 2020.

[8] B. Gottschalk, "Radiotherapy proton interactions in matter," no. arXiv:1804.00022, Mar 2018, arXiv:1804.00022 [physics]. [Online]. Available: http://arxiv.org/abs/1804.00022

[9] E. J. Lehrer, A. V. Prabhu, K. K. Sindhu, S. Lazarev, H. Ruiz-Garcia, J. L. Peterson, C. Beltran, K. Furutani, D. Schlesinger, J. P. Sheehan, and et al., "Proton and heavy particle intracranial radiosurgery," *Biomedicines*, vol. 9, no. 1, p. 31, 2021.

[10] R. L. Workman and Others, "Review of Particle Physics," *PTEP*, vol. 2022, p. 083C01, 2022.

[11] H. A. Bethe and J. Ashkin, *Passage of Radiations through Matter.* John Wiley & Sons, Inc., 1953, vol. 1, p. 789.

[12] T. Bortfeld, "An analytical approximation of the Bragg curve for therapeutic proton beams," *Medical Physics*, vol. 24, no. 12, p. 2024–2033, 1997.

[13] E. W. Weisstein, "Gamma Function." [Online]. Available: https://mathworld.wolfram.com/GammaFunction.html

[14] ——, "Parabolic Cylinder Function." [Online]. Available: https://mathworld.wolfram.com/ParabolicCylinderFunction.html

[15] J. J. Wilkens, C. Granja, C. Leroy, and I. Stekl, *Introduction to Radiotherapy with Photon and Electron Beams and Treatment Planning from Conformal Radiotherapy to IMRT.* THE 4TH INTERNATIONAL CONFERENCE ON MATERIALS ENGINEERING AND NANOTECHNOLOGY (ICMEN 2021), 2007.

[16] H. Paganetti, *Proton Beam Therapy*, ser. 2399-2891. IOP Publishing, 2017. [Online]. Available: https://dx.doi.org/10.1088/978-0-7503-1370-4

[17] A. M. Allen, T. Pawlicki, L. Dong, E. Fourkal, M. Buyyounouski, K. Cengel, J. Plastaras, M. K. Bucci, T. I. Yock, L. Bonilla, R. Price, E. E. Harris, and A. A. Konski, "An evidence based review of proton beam therapy: The report of astro's emerging technology committee," *Radiotherapy and Oncology*, vol. 103, no. 1, p. 8–11, Apr 2012.

[18] K. Parodi and W. Assmann, "Ionoacoustics: A new direct method for range verification," *Modern Physics Letters A*, vol. 30, no. 17, p. 1540025, 2015. [Online]. Available: https://doi.org/10.1142/S0217732315400258

[19] M. Xu and L. V. Wang, "Universal back-projection algorithm for photoacoustic computed tomography," *Physical Review E*, vol. 71, no. 1, 2005.

[20] B. T. Cox, S. R. Arridge, and P. C. Beard, "Photoacoustic tomography with a limited-aperture planar sensor and a reverberant cavity," *Inverse Problems*, vol. 23, no. 6, p. S95–S112, Nov 2007.

[21] B. E. Treeby, E. Z. Zhang, and B. T. Cox, "Photoacoustic tomography in absorbing acoustic media using time reversal," *Inverse Problems*, vol. 26, no. 11, p. 115003, Sep 2010.

[22] B. E. Treeby and B. T. Cox, "k-Wave: MATLAB toolbox for the simulation and reconstruction of photoacoustic wave fields," *Journal of Biomedical Optics*, vol. 15, no. 2, p. 021314, 2010.

[23] J. Zhang, K. Wang, Y. Yang, and M. A. Anastasio, "Simultaneous reconstruction of speed-of-sound and optical absorption properties in photoacoustic tomography via a time-domain iterative algorithm," in *Photons Plus Ultrasound: Imaging and Sensing 2008: The Ninth Conference on Biomedical Thermoacoustics, Optoacoustics, and Acousto-optics*, A. A. Oraevsky and L. V. Wang, Eds., vol. 6856. SPIE, 2008, p. 427–434, backup Publisher: International Society for Optics and Photonics. [Online]. Available: https://doi.org/10.1117/12.764171

[24] W. Assmann, S. Kellnberger, S. Reinhardt, S. Lehrack, A. Edlich, P. G. Thirolf, M. Moser, G. Dollinger, M. Omar, V. Ntziachristos, and K. Parodi, "Ionoacoustic characterization of the proton bragg peak with submillimeter accuracy," *Medical Physics*, vol. 42, no. 2, pp. 567–574, 2015. [Online]. Available: https://aapm.onlinelibrary.wiley.com/doi/abs/10.1118/1.4905047

[25] J. Lascaud, P. Dash, H.-P. Wieser, R. Kalunga, M. Würl, W. Assmann, and K. Parodi, "Investigating the accuracy of co-registered ionoacoustic and ultrasound images in pulsed proton beams," *Physics in Medicine & Biology*, vol. 66, no. 18, p. 185007, Sep 2021.

[26] J. Lascaud, R. Kalunga, S. Lehrack, H.-P. Wieser, F. S. Englbrecht, M. Wurl, W. Assmann, A. S. Savoia, and K. Parodi, "Applicability of capacitive micromachined

ultrasonic transducers for the detection of proton-induced thermoacoustic waves," in *2019 IEEE International Ultrasonics Symposium (IUS)*. Glasgow, United Kingdom: IEEE, Oct 2019, p. 143–146. [Online]. Available: https://ieeexplore.ieee.org/document/8926023/

[27] J. Lascaud, R. Kowalewski, B. Wollant, H. Carmigniani, K. Schnurle, P. Dash, H.-P. Wieser, J. Bortfeldt, R. Kalunga, R. Rouffaud, A. Gerard, M. Vidal, J. Herault, D. Certon, and K. Parodi, "Optimization of the backing material of a low frequency pvdf detector for ion beam monitoring during small animal proton irradiation," in *2021 IEEE International Ultrasonics Symposium (IUS)*. Xi'an, China: IEEE, Sep 2021, p. 1–4. [Online]. Available: https://ieeexplore.ieee.org/document/9593703/

[28] G. F. Knoll, *Radiation detection and measurement*, 4th ed. Hoboken, N.J: John Wiley, 2010.

[29] J. B. Birks, *The Theory and practice of scintillation counting*. Pergamon Press Limited, 1964.

[30] R. Craun and D. Smith, "Analysis of response data for several organic scintillators," *Nuclear Instruments and Methods*, vol. 80, no. 2, p. 239–244, Apr 1970.

[31] L. Kelleter and S. Jolly, "A mathematical expression for depth-light curves of therapeutic proton beams in a quenching scintillator," *Medical Physics*, vol. 47, no. 5, p. 2300–2308, May 2020.

[32] D. Lo Presti, G. Gallo, D. Luigi Bonanno, D. Giuseppe Bongiovanni, F. Longhitano, and S. Reito, *Real-Time Particle Radiography by Means of Scintillating Fibers Tracker and Residual Range Detectors*. IntechOpen, Apr 2019. [Online]. Available: https://www.intechopen.com/books/applications-of-optical-fibers-for-sensing/real-time-particle-radiography-by-means-of-scintillating-fibers-tracker-and-residual-range-detectors

[33] *PTW User Manual Water Phantom T41023*, PTW, Sep 2009, d738.131.00/02 en.

[34] S. Agostinelli, J. Allison, K. Amako, J. Apostolakis, H. Araujo, P. Arce, M. Asai, D. Axen, S. Banerjee, G. Barrand, and et al., "Geant4—a simulation toolkit," *Nuclear*

Instruments and Methods in Physics Research Section A: Accelerators, Spectrometers, Detectors and Associated Equipment, vol. 506, no. 3, pp. 250–303, 2003. [Online]. Available: https://www.sciencedirect.com/science/article/pii/S0168900203013688

[35] M. T. Studenski, "Proton therapy dosimetry using positron emission tomography," *World Journal of Radiology*, vol. 2, no. 4, p. 135, 2010.

[36] S. M. Vatnitsky, "Radiochromic film dosimetry for clinical proton beams," *Applied Radiation and Isotopes*, vol. 48, no. 5, p. 643–651, May 1997.

[37] M. Kawashima, A. Matsumura, H. Souda, and M. Tashiro, "Simultaneous determination of the dose and linear energy transfer (let) of carbon-ion beams using radiochromic films," *Physics in Medicine & Biology*, vol. 65, no. 12, p. 125002, Jun 2020.

[38] S. Vynckier, D. Bonnett, and D. Jones, "Code of practice for clinical proton dosimetry," *Radiotherapy and Oncology*, vol. 20, no. 1, p. 53–63, Jan 1991.

[39] J. Medin, P. Andreo, and S. Vynckier, "Comparison of dosimetry recommendations for clinical proton beams," *Physics in Medicine and Biology*, vol. 45, no. 11, p. 3195–3211, Nov 2000.